Research
Air Pollution Control—Article

# The Significant Contribution of Small-Sized and Spherical Aerosol Particles to the Decreasing Trend in Total Aerosol Optical Depth over Land from 2003 to 2018

Ke Gui [a], Huizheng Che [a,*], Lei Li [a], Yu Zheng [a], Lei Zhang [a], Hujia Zhao [b], Junting Zhong [a], Wenrui Yao [a], Yuanxin Liang [a], Yaqiang Wang [a], Xiaoye Zhang [a]

[a] State Key Laboratory of Severe Weather & Key Laboratory of Atmospheric Chemistry of China Meteorological Administration, Chinese Academy of Meteorological Sciences, Beijing 100081, China
[b] Institute of Atmospheric Environment, China Meteorological Administration, Shenyang 110166, China

## ARTICLE INFO

## ABSTRACT

The optical and microphysical properties of aerosols remain one of the greatest uncertainties associated with evaluating the climate forcing attributed to aerosols. Although the trends in aerosol optical depth (AOD) at global and regional scales have been widely examined, little attention has been paid to the trends in type-dependent AODs related to aerosol particle properties. Here, using the aerosol optical component dataset from the Multi-angle Imaging SpectroRadiometer (MISR) instrument, we investigate decadal-scale trends in total aerosol loading as well as AODs for five aerosol components by particle size and morphology during 2003–2018 over land. Relationships between the total AOD (TAOD) trends and type-dependent AOD changes were examined, and the relative contribution of each type-dependent AOD to the overall TAOD trends was quantified. By dividing the TAOD values into four different aerosol pollution levels (APLs) with splits at 0.15, 0.40, and 0.80, we further explored the relationships between TAOD changes and interannual variations in the frequency-of-occurrences (FoOs) of these APLs. Long-term trends in FoOs in the different APLs show that there was a significant improvement in air quality between 2003 and 2018 in most land areas, except South Asia, corresponding to a shift from lightly polluted to clean conditions. However, the effects of different APLs on TAOD changes are regionally dependent and their extent of correlation varied spatially. Moreover, we observed that the annual mean TAOD has decreased by $0.47\%\cdot a^{-1}$ over land since 2003 ($P < 0.05$). This significant reduction was mainly attributed to the continued reduction in small-sized (< 0.7 mm diameter) AOD (SAOD) ($-0.74\%\cdot a^{-1}$) and spherical AOD (SPAOD) ($-0.46\%\cdot a^{-1}$). Statistical analysis shows that SAOD and SPAOD respectively accounted for 57.5% and 89.6% of the TAOD, but contributed 82.6% and 90.4% of the trend in TAOD. Our study suggests that small-sized and spherical aerosols composed of sulfate, organic matter, and black carbon play a dominant role in determining interannual variability in land TAOD.

## 1. Introduction

As a key perturbation quantity in the Earth's climate system, atmospheric aerosols (AAs) from anthropogenic or natural sources have been shown to affect weather, climate, and the environment on global to regional scales to varying degrees through mechanisms such as aerosol–radiation and aerosol–cloud interactions [1–11]. Moreover, AAs (especially fine particulate matter (PM$_{2.5}$)

near the surface) have adverse health effects when inhaled into the human body because they contain toxic substances that affect the respiratory and circulatory systems, potentially increasing morbidity and mortality [12–15].

Aerosol optical depth (AOD), defined as the integral of the extinction coefficient of AAs along the entire atmospheric column, describes the overall attenuation of solar radiation by AAs. As one of the critical variables for characterizing atmospheric aerosol loading, AOD has been widely applied to examine atmospheric pollution characteristics at urban, regional, and global scales, and to assess its effects on radiation, precipitation, and clouds [1,16–19].

Numerous studies have been conducted to investigate the interannual and intra-annual variability of AOD at global to regional scales using ground-based observations, satellite remote sensing, and numerical modeling, and to explore their relationships with anthropogenic emissions, meteorological factors, and climate forcing [20–23]. However, little attention has been paid to the interannual variation in the frequency-of-occurrences (FoOs) of different aerosol loading levels and its implications for the variation in total aerosol loading. Different aerosol loadings are associated with different aerosol pollution levels (APLs), and their changes can clearly indicate the degree of improvement or deterioration of air quality. Thus, the magnitude of adverse health effects caused by aerosols is not only induced by interannual concentration changes, but also strongly depends on the frequency of human exposure to different aerosol pollution loadings.

Regional aerosol particles are influenced by several factors such as geographic location, topography, surface properties, population density, proximity of pollution sources, and meteorological conditions, resulting in large differences in their concentration, size distributions, morphology, chemical compositions, and optical properties [23,24]. As a result, even for the same AOD, different aerosol types with a wide range of size distributions and complex morphology have different effects on the magnitude and sign of aerosol radiative forcing [18,25]. Correspondingly, in addition to total AOD (TAOD), a systematic analysis of the interannual variability of AODs due to different aerosol types at global and regional scales is essential to enhance our knowledge of aerosol climatic and environmental effects. This knowledge will also help us to better distinguish the role of natural and anthropogenic aerosols in driving interannual variability in total aerosol loading.

In this study, we investigated the interannual variability and trends in land total aerosol loadings and type-dependent AODs related to aerosol particle properties (i.e., size and morphology) using the latest Multi-angle Imaging SpectroRadiometer (MISR) V23 aerosol component products during 2003–2018 and explored the effects and relative contributions of these type-dependent AODs to TAOD changes. In addition, by categorizing the TAOD values into four different APLs with splits at 0.15, 0.40, and 0.80, we further examined the climatological characteristics and variability of the FoOs at these APLs. The objectives of this study were as follows: ① to identify the dominant aerosol types driving the decadal variations in TAOD at land and regional scales in terms of aerosol microphysical properties (i.e., particle size and morphology); and ② to understand the spatiotemporal variations in the FoOs of different APLs.

## 2. Data and methodology

### 2.1. MISR aerosol component products

The MISR sensor, which is onboard the Terra satellite, can provide near-global coverage once every nine days [26]. MISR observes the Earth's atmosphere at four visible or near-infrared spectral bands along nine orbital viewing angles, which allow it to categorize aerosol loadings by particle type and provide detailed aerosol particle property information [27]. In this study, we used the Level-3 (gridded) monthly global aerosol component products (MIL3MAEN) from the latest release version F15_0032 during 2003–2018. MISR Level-3 aerosol component data are provided at $0.5° \times 0.5°$ spatial resolution, based on the higher resolution (4.4 km) Level-2 (swath) aerosol product. Compared with the previous version of the algorithm (V22), the MISR data products based on the latest algorithm (V23) provide significant improvements in both accuracy and resolution [28]. The V23 dataset was produced by two separate retrieval algorithms: the heterogeneous surface

(Het Surf) algorithm, which is applied to land surfaces, and the dark water algorithm, which is applied to the ocean or deep inland water [29].

The parameters used in the study were the TAOD at 550 nm as well as the AODs for three different particle size groups—namely, small (< 0.7 μm diameter), medium (0.7–1.4 μm diameter), and large (> 1.4 μm diameter)—and for two different particle shapes—namely, spherical and non-spherical. Hereafter, small, medium, large, spherical, and non-spherical AODs are referred to as SAOD, MAOD, LAOD, SPAOD, and NSPAOD, respectively. Note that the V23 of the MISR product does not provide SPAOD directly; rather, it must be obtained by the difference between TAOD and NSPAOD. Particle size classifications in MISR are based on predefined particle types described by a log-normal distribution and are characterized by their characteristic width parameters and radius [30]. The classifications of these three modes are different from the two-mode description in most aerosol optical properties studies, which only distinguishes between fine and coarse modes. Moreover, using the particle property retrieval algorithm, MISR separates the NSPAOD from the TAOD. Evaluation of the MISR V23 Level-2 AOD product with the ground-based measurements of Aerosol Robotic Network (AERONET) suggested significant agreement over land (correlation coefficient ($R$) = 0.81 and root–mean-square error = 0.154) [28]. Further statistical results show that 66.1% of the matched samples of the MISR-retrieved AOD values fall within 0.03 or 10% × AOD of the AERONET [28]. More importantly, the MISR V23 AOD product has acceptable accuracy even at low-AOD ranges (i.e., AOD < 0.1) because the unrealistic quantification of low AOD in the MISR V22 AOD product has been largely eliminated from V23 [28]. Unlike TAOD, the valuation of the accuracy of aerosol particle properties is more challenging, in part because both ground-based and aircraft validation data for MISR are very sparse and the sensitivity of remote sensing to particle properties is much more dependent than AOD on retrieval conditions. Nevertheless, the analysis of retrieval constraints on particle size and shape conducted by Kahn and Gaitley [31] largely confirmed the results of pre- and post-launch theoretical sensitivity studies [32]. In addition, individual case studies show that there is good discrimination between non-spherical dust and spherical particles in field observations.

### 2.2. MODIS, MERRA-2, and CAMS AOD products

We also examined the annual trend in total aerosol loading over land during the same overlapping period as MISR using the monthly gridded AOD data at 550 nm (combined Dark Target and Deep Blue algorithms, MOD08_M3 and MYD08_M3) with a spatial resolution of $1° \times 1°$, observed by MODIS/Terra and MODIS/Aqua. Similar analyses were also performed using the Copernicus Atmosphere Monitoring Service (CAMS) and the Modern-Era Retrospective Analysis for Research and Applications, version 2 (MERRA-2) aerosol reanalysis products. CAMS is the latest global atmospheric composition reanalysis dataset generated by the European Centre for Medium-Range Weather Forecasts (ECMWF) and consists of atmospheric composition fields including major precursors, chemical species, and aerosols [33]. MERRA-2 is a second-generation atmospheric aerosol reanalysis of the new modern satellite era (post-1980), which assimilates both meteorological observations and the AODs from various ground- and satellite-based observations [34]. The spatial resolutions of the CAMS and MERRA-2 AOD fields are $0.75° \times 0.75°$ and $0.500° \times 0.625°$, respectively. On the land average (Fig. S1 in Appendix A), MISR shows acceptable synergy with the other four datasets, with $R$ ranging from 0.60 to 0.83.

To explore the role of anthropogenic and natural aerosols in driving interannual variability in total aerosol loading, we used

the AODs for five aerosol components from the CAMS reanalysis, including sulfate (SU), dust (DU), black carbon (BC), organic matter (OM), and sea salt (SS). In this study, we define SU, BC, and OM as anthropogenic fine-mode aerosols (SU + BC + OM), whereas DU and SS are described as natural coarse-mode aerosols (DU + SS). To perform the spatial analysis, the MISR dataset at high spatial resolution ($0.5° \times 0.5°$) was bilinearly interpolated to the CAMS resolution of $0.75° \times 0.75°$.

### 2.3. Definition of the FoO of APLs

By counting the number of Level-2 available daily AOD retrievals within each $0.5° \times 0.5°$ grid box, MISR's Level-3 AOD product stores the monthly cumulative number of occurrences of eight AOD intervals. In general, different TAOD ranges usually correspond to different APLs. In this study, the APLs are categorized as having clean (APL 1), lightly polluted (APL 2), moderately polluted (APL 3), and heavily polluted (APL 4) conditions, with the corresponding TAOD values of < 0.15, 0.15–0.40, 0.40–0.80, and > 0.80, respectively. By quantifying the FoO of these four different APLs, we were able to explore their climatology, trends, and links to changes in TAOD. The FoO (%) for each APL is defined as follows:

$$FoO = \frac{N_{APL}}{N_{all\ APLs}} \times 100\% \tag{1}$$

where $N_{APL}$ and $N_{all\ APLs}$ represent the cumulative samples of specified APL and all APL occurrences, respectively. In general, the spatio–temporal evolution in TAOD reflects the variations in columnar aerosol concentrations, but it is difficult to characterize the changes in different aerosol concentration levels. Therefore, quantifying the FoOs from APL 1 to APL 4 at each grid point will provide insight into the distribution characteristics of different APLs at the global scale, since the magnitude of the adverse health effects caused by aerosols is usually closely related to the frequency of human exposure to different aerosol pollution loadings.

### 2.4. Correlation and trend analysis

In this study, Pearson's *R* was used to explore the relationships between TAOD trends and interannual variations in the type-dependent AODs and the FoOs of different APLs. Two-tailed Student's *t*-tests were used to assess the robustness of the correlation, and statistical significance was set at the 95% confidence level (i.e., $P < 0.05$). The trend analysis was carried out for the TAOD and AODs by different aerosol types at both the global and regional scales using the Mann–Kendall (M–K) $\tau$ test [35,36] with Sen's slope method. To ensure the robustness of the trend assessment, we required that at least 60% of the data in each annual time series be valid before the trend calculations could be performed. When calculating the annual time series, it is necessary to ensure that the length of the valid monthly time series is greater than 60%. The M–K trend test is a nonparametric method with the advantage that data samples do not have to follow a particular probability distribution and are rarely disturbed by "outliers." In this study, Sen's slope was applied to evaluate the strength of the trend value; then, the M–K statistical test was employed to test whether these estimated trends were significant at a given significance level (interested readers can refer to Text S1 in Appendix A for detailed procedures of trend estimation and the M–K statistical tests).

### 2.5. Isolating the relative contribution of type-dependent AODs

In MISR's retrieval algorithm, the TAOD can be expressed as follows:

$$TAOD = \sum_{i=1}^{3} \beta_i \times AOD_{size}^i = \sum_{i=1}^{2} \partial_i \times AOD_{shape}^i \tag{2}$$

where $AOD_{size}^i$ and $AOD_{shape}^i$ represent each size-segregated AOD (i.e., large, medium, and small AODs) and shape-segregated AOD (i.e., spherical and non-spherical AODs), respectively; and $\beta_i$ and $\partial_i$ are weighting coefficients (both equal to 1). The relative contribution (RC, %) of each size-segregated (shape-segregated) AOD to the TAOD trend was estimated through a comparison with the TAOD change:

$$RC^i = \frac{\Delta^i}{\Delta_{TAOD}} \times 100\% \tag{3}$$

where $\Delta^i$ and $\Delta_{TAOD}$ represent the linear change for each size-segregated or shape-segregated AOD and TAOD, respectively. Linear changes were determined by the slope of ordinary least-squares linear regression, and two-tailed Student's *t*-tests were used to detect whether the slopes were significant at the 95% confidence level. For RCs, the positive (negative) sign of the RC indicates that type-dependent AOD changes exhibit a facilitating (offsetting) effect on the TAOD trend. Furthermore, the non-negative RCs (NRCs) of size-segregated and shape-segregated AOD, respectively, were obtained using Eqs. (4) and (5) below.

$$NRC_{size}^i = \frac{\left|RC_{size}^i\right|}{\sum_{i=1}^{3} \left|RC_{size}^i\right|} \times 100\% \tag{4}$$

$$NRC_{shape}^i = \frac{\left|RC_{shape}^i\right|}{\sum_{i=1}^{2} \left|RC_{shape}^i\right|} \times 100\% \tag{5}$$

In this study, we considered the RC or NRC to be significant only when the change values for TAOD and type-dependent AODs were both significant at the 95% confidence level. Using Eqs. (3)–(5), the annual RC and NRC of each size-segregated or shape-segregated AOD were separately calculated for each $0.5° \times 0.5°$ grid box for the period 2003–2018. Similarly, by applying the above method, the RC of the composition-dependent AODs (i.e., SU, BC, OM, DU, and SS) based on CAMS reanalysis was isolated.

### 2.6. Sub-regions

Because atmospheric aerosols have large spatiotemporal variability, it is essential to explore the inhomogeneity in the spatial distribution of aerosols and the consequent regional effects. Therefore, in addition to the global land perspective, we particularly focus herein on characterizing regional type-dependent AOD distributions and variability over the 14 sub-regions (SRs): North America (NAM), Central America (CAM), South America (SAM), Europe (EUR), North Africa (NAF), South Africa (SAF), the Middle East (MDE), Russia (RUS), Central Asia (CAS), South Asia (SAS), East Asia (EAS), the Indochina Peninsula (ICP), Southeast Asia (SEA), and Australia (AUS). Results from the Antarctica and Greenland regions were excluded because the Het Surf algorithm performs poorly for homogeneous regions that are largely covered with ice or snow [28]. The geographic boundaries of these SRs are indicated by different color blocks in Fig. S2 in Appendix A. Overall, compared with the global land average (Fig. S1), MISR shows good consistency with other AOD products in terms of year-to-year variation over all SRs, albeit with slight differences in magnitude (Fig. S3 in Appendix A). Specifically, among the 14 SRs, the *R* between MISR and MODIS/Terra, MODIS/Aqua, MERRA-2, and CAMS varies from 0.28 to 0.99, 0.40 to 0.98, 0.44 to 0.95, and 0.45 to 0.98, respectively.

## 3. Results and discussion

### 3.1. Global distributions of type-dependent AODs

Fig. 1(a) shows the distributions of the multi-year (2003–2018) mean AODs for size-segregated (large, medium, and small) and shape-segregated (spherical and non-spherical) aerosols. Overall, among the size-segregated aerosols, small-sized aerosols contributed the most to aerosol extinction over land, with a multi-year average TAOD of 0.093, followed by large- and medium-sized aerosols with land-average AODs of 0.057 and 0.023, respectively. To be specific, LAODs were mainly distributed in the lower latitudes of the Northern Hemisphere (0–30 °N), with enhancements (about 0.2–0.3) located mainly in dust-source areas (including the Sahara Desert, Saudi Arabian Desert, and Taklimakan Desert) and in regions of high anthropogenic emissions, such as northern India and eastern China (EC). The distribution pattern of MAODs was similar to that of LAODs, but the intensities of high MAOD loading were about half those of LAODs. In contrast, high SAODs were widespread over most of the land area of the world and had complex contributors, including a fine fraction of natural mineral dust in desert-source areas, fine or ultrafine modes of strongly absorbing aerosols emitted from typical biomass-burning regions, and urban and industrial aerosols from areas with high anthropogenic emissions. In terms of aerosol morphology, spherical aerosols completely dominated global aerosol extinction over land, with a global average value (0.149) about six times higher than that of non-spherical aerosols (0.024). In general, sea salt particles, smoke aerosols, and secondary aerosols generated by air pollution are close to spherical, while coarse particles such as dust aerosols and biological debris (e.g., pollen) are non-spherical aerosols. Therefore, the global distribution pattern of NSPAODs was very similar to that of LAODs and MAODs, particularly in desert-source regions.

We further calculated the annual proportion of the multi-year mean AODs by different particle types to the TAOD (Fig. 1(b)). As a global average, small-sized aerosols contributed the largest proportion of the multi-year average TAOD (57.5%), followed by large-sized aerosols (32.2%), while medium-sized aerosols (10.3%) contributed the smallest proportion. From the perspective of aerosol shape, we found that spherical and non-spherical aerosols contributed 89.6% and 10.4% of the TAOD, respectively. Specifically,
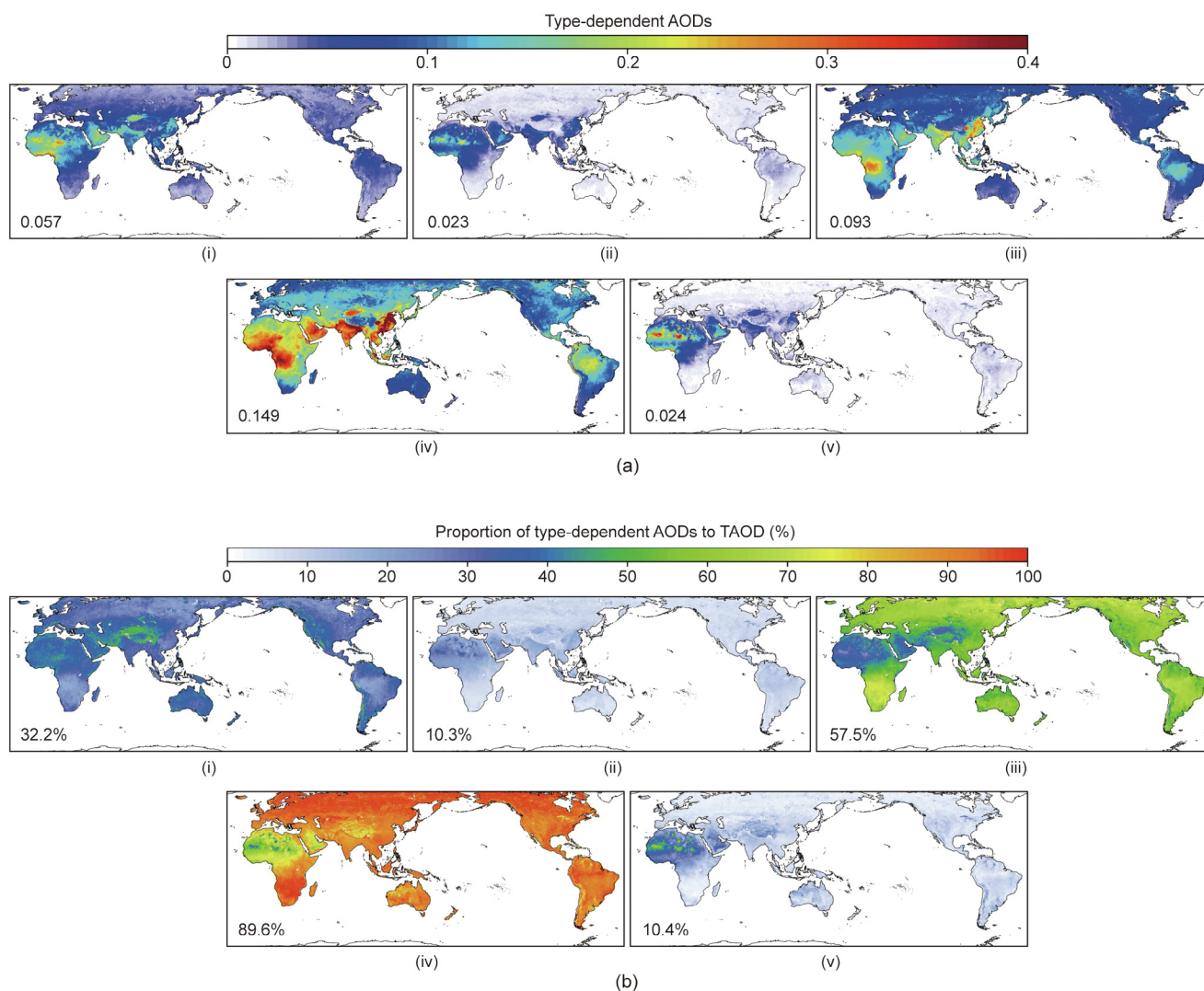


**Fig. 1.** Climatological distributions of (a) type-dependent AODs and (b) type-dependent AODs as a proportion of TAOD during 2003–2018. (i) Large-sized, (ii) medium-sized, (iii) small-sized, (iv) spherical, and (v) non-spherical. The proportion given in the lower left of each panel represents the land average corresponding to the individual variable.

as illustrated in Fig. 1(b-i), the proportion of LAOD to TAOD (P_LAOD) was generally less than 50% in other land areas except for the Sahara Desert, East Arabian Peninsula, Iranian Highlands, northwestern China, and the southeastern Tibetan Plateau, China (TP). It is noteworthy that over the TP, the multi-year average P_LAOD was about 40%–60%, which can be mainly attributed to the long-range transport of dust aerosols [37]. As a result of the narrow particle size range (0.7–1.4 μm diameter) and limited aerosol sources, variations in the proportion of MAOD to TAOD (P_MAOD) over land were not prominent, except for the NAF region, where the P_MAOD was around 30%–40%. For small-sized aerosols, the enhanced proportion of SAOD to TAOD (P_SAOD) (> 70%) was mainly located in typical biomass-burning regions, including Central and North America, SAM, SAF, and Eastern Siberia. Unlike the distribution of size-segregated AOD, spherical aerosols contributed almost 90% of the total aerosol extinction over land areas other than NAF, MDE, and the TP. In contrast, the Sahara Desert region was the largest contributor of land non-spherical aerosol types, as it caused about 30%–60% of the total aerosol extinction.

### 3.2. Climatology and trends of the FoOs for different APLs

As clearly depicted in Fig. 2(a), distinctly different land distribution characteristics can be observed between the climatology of the FoOs for different APLs. Overall, the FoOs tended to decrease progressively with increasing aerosol loading over the land areas. The land-average FoOs for APL 1 to APL 4 were 63.1%, 26.9%, 8.5%, and 1.6%, respectively. For APL 1 (TAOD < 0.15; considered as clean condition), the high FoOs were mainly located in areas far from natural and anthropogenic aerosol pollution, and ranged from 80% to 100%. It should be noted that the FoOs of APL 1 were less than 5% in North–Central Africa, MDE, northern SAS, and east–central China, indicating that people in these regions are exposed to varying degrees of aerosol pollution all year round. For APL 2 (0.15 < TAOD < 0.40; considered as lightly polluted), the intensification of multi-year annual average FoOs (about 50%–70%) was located mainly in northern SAM, NAF, the MDE, CAS, SAS, SEA, and Chinese mainland, except for the TP. Remarkably, the FoO for APL 2 was about 0–30% over the TP, indicating that the region is also susceptible to varying degrees of aerosol pollution. Previous studies have suggested that aerosols over the TP are mainly transported from surrounding areas, including springtime dust aerosols from the Taklamakan Desert and anthropogenic aerosols in SAS [37,38]. These aerosols have been confirmed to play a key role in the weather and climate system over the TP through aerosol–radiation and aerosol–cloud interactions [39].

Compared with the spatial distribution pattern of the FoO for APL 2, the FoO for APL 3 (0.40 < TAOD < 0.80; considered as moderately polluted) presented a similar distribution with attenuated intensity, and the extent of its high-value area was significantly reduced or even shifted. For example, the highest FoO (> 60%) was mainly distributed in Central Africa and northern India, with the former mainly being attributed to frequent biomass-burning events from summer to winter [40] and the latter to enhanced persistent anthropogenic emissions [41]. The second-highest FoOs (about 20%–50%) were found in NAF, the MDE, southern India, eastern and northwestern China, and ICP, while the third-highest FoOs (10%–20%) were found in regions such as central SAM, with forest wildfires as the dominant contributor [42]. In contrast, the
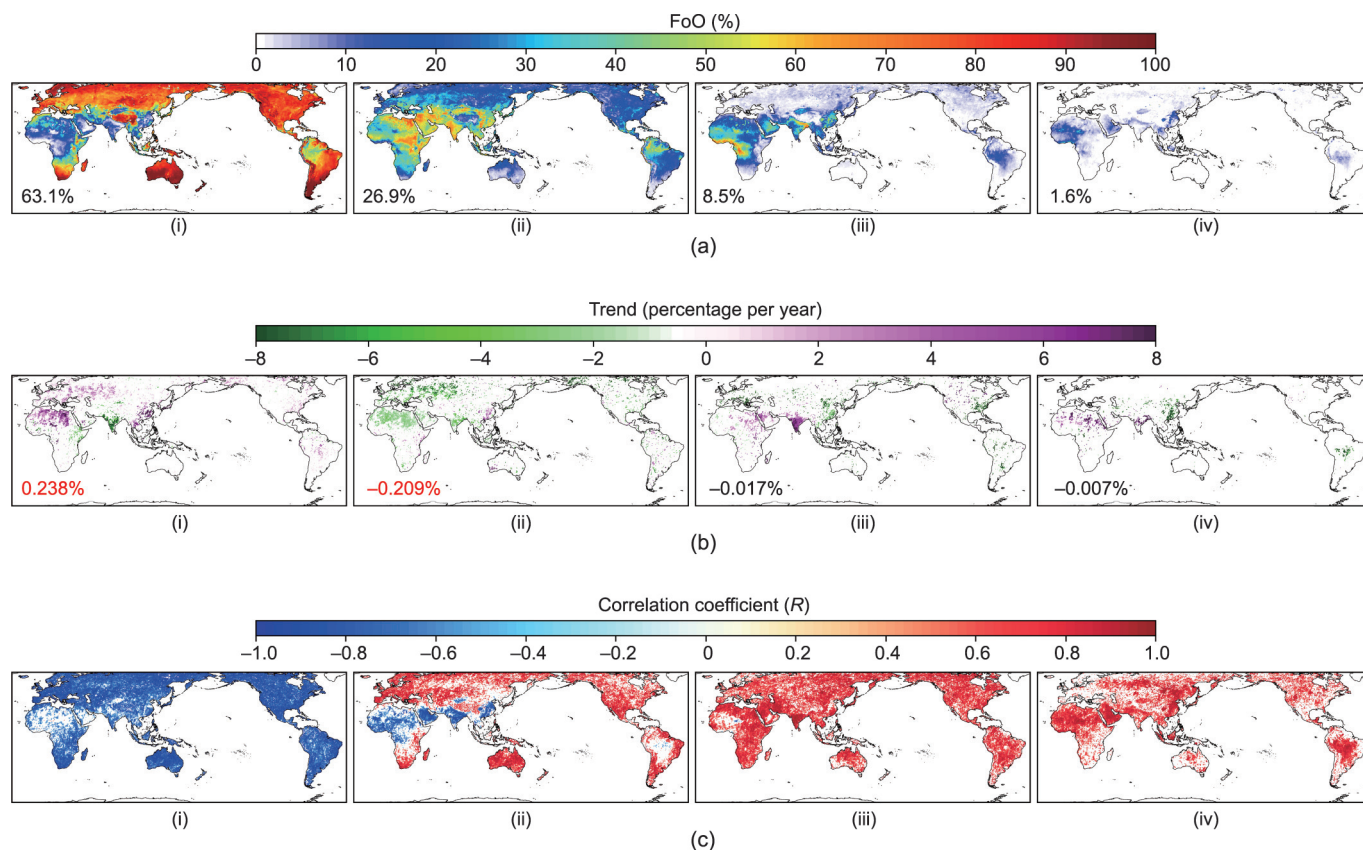


**Fig. 2.** (a) Climatological distributions of the FoOs for different APLs during the period 2003–2018. The number in the lower left of each panel represents the land average of the FoO. (b) The annual trends in FoOs, expressed as a percentage change: $\frac{\text{slope}}{\bar{y}} \times 100\%$, where slope represents Sen's slope and $\bar{y}$ represents the annual mean value. The number in the lower left of each panel represents the percentage trend value calculated from the time series of the land annual average. Note that numbers marked in red indicate that the trend values are above the 95% significance level from the M–K test. (c) The correlation coefficients ($R$) for the TAOD versus FoOs (note that only grid cells with $R$ above 95% significance level are shown). (i) ALP 1, (ii) APL 2, (iii) APL 3, and (iv) APL 4.

FoO for APL 4 (TAOD > 0.80; considered as heavily polluted) exhibited a clear and distinct spatial distribution, successfully capturing several well-known areas of high aerosol pollution around the world [23], dominated by different aerosol types. For example, NAF and the MDE were dominated by mineral dust aerosols, north China and the Sichuan Basin were dominated by anthropogenic aerosols, and Central Africa, central SAM, ICP, and SEA were dominated by biomass-burning aerosols. These findings suggest that the people in these regions experienced the world's worst atmospheric ambient conditions for about 10%–20% of days during 2003–2018. The spatial distribution of these pollution hotspots is consistent with the high value of surface $PM_{2.5}$ concentrations estimated from satellite-retrieved AOD [43].

Quantifying long-term variations in different APLs contributes to revealing the historical evolution of the FoOs in humans exposed to different APLs. Therefore, we further estimated the trends in the FoOs of different APLs, as shown in Fig. 2(b). The temporal trend results show that the trend distribution patterns were very distinct among different APLs. Globally, we found a 0.238%·a$^{-1}$ ($P$ < 0.05) increase in the FoO in APL 1 over land during 2003–2018. In other words, the number of days with clean aerosol conditions increased by 3.8% over the study period, indicating that air quality improved dramatically in most regions over land, although a few zones (e.g., SAS and East–Central Africa) exhibit negative trends. Spatially, the significant increase (about 2%–8% per year) in the FoO in APL 1 occurred predominantly in NAF, the entire EUR, eastern NAM, central SAM, and EAS. However, the significant negative trend in SAS and East–Central Africa means that air quality gradually deteriorated over the study period.

Compared with the trend distribution of APL 1, the trend signs of APL 2 reversed sharply in all regions except for SAS and EAS, where it did not change significantly. The widespread negative trend directly contributed to a 0.209%·a$^{-1}$ ($P$ < 0.05) decrease in the FoO in APL 2 over land.

Unlike APLs 1 and 2, there was a set of completely opposing regional trends for the FoO in APL 3, in which clearly identifiable positive trends were located in SAS, the MDE, and eastern NAF, and negative trends were located in eastern NAM, South–Central EUR, and EC. Globally, the above regional contrasting trends determine a non-significant decline (−0.017%·a$^{-1}$) over land at a global scale.

Similar to APL 3, APL 4 reveals regional trends that were equally opposing (compared with APLs 1 and 2) but with a reduced extent of influence. To be specific, compared with the trend pattern of APL 3, the increasing trend of APL 4 was stronger and more extensive in NAF, while the magnitude of the decline became more intensified and clustered in EC. In contrast, unlike the APL 3 trend, which had a positive sign across SAS, APL 4 had a significant reduction in the coverage of its positive trend. A similar shift was also observed in the MDE. Furthermore, APL 4 showed an unusually prominent decreasing trend in central SAM. These regionally significant trends contributed to a non-significant slight decline (−0.007%·a$^{-1}$) in APL 4 at the global scale. Remarkably, the decreased APLs 3 and 4 and increased APL 2 in EC are also supported by the results obtained by Zhang et al. [44] using long-term ground-based observations; that is, the frequency of heavy haze events in EC has significantly decreased, but the frequency of light/moderate haze events has not shown a decreasing trend. Zhang et al. [44] reported that the declined frequency of heavy haze events could mainly be attributed to significantly reduced sulfur dioxide ($SO_2$) in EC [45–49]; however, specific chemical reaction mechanisms (i.e., catalytic reactions on the surface of BC) at low $SO_2$ conditions prevent the reduction of the frequency of light/moderate haze events. In order to implement a reduction in the frequency of light/moderate haze events, synergistic measures such as controlling both $SO_2$ and primary BC, along with sustained reductions in other

primary gases and aerosols [44], are needed to significantly reduce the levels of regional total aerosol loading.

The probability density function (PDF) of trends in APLs, TAOD and size-segregated AODs, and TAOD shape-segregated AODs were shown in Fig. 3. The PDFs calculated for each APL on all grids over land with statistically significant trend values shows that APLs 1 and 2 exhibited two opposing single-peaked distribution modes (peaks of 2.06%·a$^{-1}$ and −2.77%·a$^{-1}$, respectively), indicating a transition from light pollution to clean conditions in land air quality (Fig. 3(a)). The interannual variation in land FoOs at different APLs also presents this transition process in detail (Fig. S4 in Appendix A). In contrast, the similar bimodal distributions of APLs 3 and 4 promote and offset (corresponding to the left and right peaks) to some extent the degree of improvement in clean conditions. By comparing the trend patterns of different APLs over pollution hotspot regions, we further characterized the evolution of these regional trends in APLs as follows: ① The decrease in the FoOs of APLs 3 and 4 in EC facilitated the increase in APLs 1 and 2; ② the increase in the FoOs of APLs 3 and 4 in SAS resulted in the decrease in APLs 1 and 2; ③ the decrease in the FoOs of APLs 2 and 3 in EUR and eastern NAM facilitated the increase in APL 1; and ④ the decrease of APL 2 in NAF and the MDE promoted the increase in APLs 1, 3, and 4.

To determine which APL dominates the interannual variation in regional TAOD, we explored the relationship between APLs and TAOD by performing a correlation analysis, as shown in Fig. 2(c). Overall, two opposing relationship patterns were found. Specifically, there was a significant negative correlation between TAOD and APL 1 over almost all land regions, except for a dust belt (extending from the west coast of North Africa and passing across the MDE and SAS, to northwest China), which showed an insignificant correlation. However, these significant negative correlations (insignificant correlations) were completely reversed between TAOD and APL 2, showing a significant positive (negative) correlation. At the same time, compared with the correlation patterns between TAOD and APLs 1 and 2, the significant positive correlations between TAOD and APLs 3 and 4 covered almost all regions of the world. The above results show that the effects of the variation in FoOs at different APLs on the interannual evolution of TAOD were complex and strongly regionally dependent. Taken together, these effects can be briefly summarized as follows: ① Changes in APL 1 had negligible effects on the interannual evolution of TAOD in dust-source and high-anthropogenic-emission regions; instead, it was mainly influenced by the FoOs for APLs 2–4. ② There were significant regional differences in the effects of FoOs on TAOD. For example, over the TP, the variation in TAOD was mainly regulated by the FoOs of APLs 1–3. In NAF, it was mainly controlled by APLs 2–4. In the central SAM, it was mainly dominated by APLs 1, 3, and 4. ③ APLs 2–4 exhibited different degrees of dominant driving role in natural or anthropogenic pollution source areas and their adjacent regions.

### 3.3. Long-term trends in type-dependent AODs

Regional changes in AODs by different particle types are usually closely related to the variations in local anthropogenic aerosols driven by the intensity of human activities and natural aerosols (e.g., DU and SS) driven by meteorological conditions. Thus, quantifying the interannual evolution of AODs by different particle types can provide a useful reference for estimating global and regional trends in anthropogenic and natural aerosols. Fig. S5 in Appendix A and Fig. 4(a) show the estimated annual trends in TAOD and size-segregated AODs globally. We observed a 0.47%·a$^{-1}$ decrease (i.e., a decline of 7.5% in the studied 16 years) in TAOD during 2003–2018. Spatially, the regions in which the TAOD trends experienced a significant decrease (roughly 1%–5% per year) were mainly located in northwest and eastern NAM, central SAM, EUR, and EC,
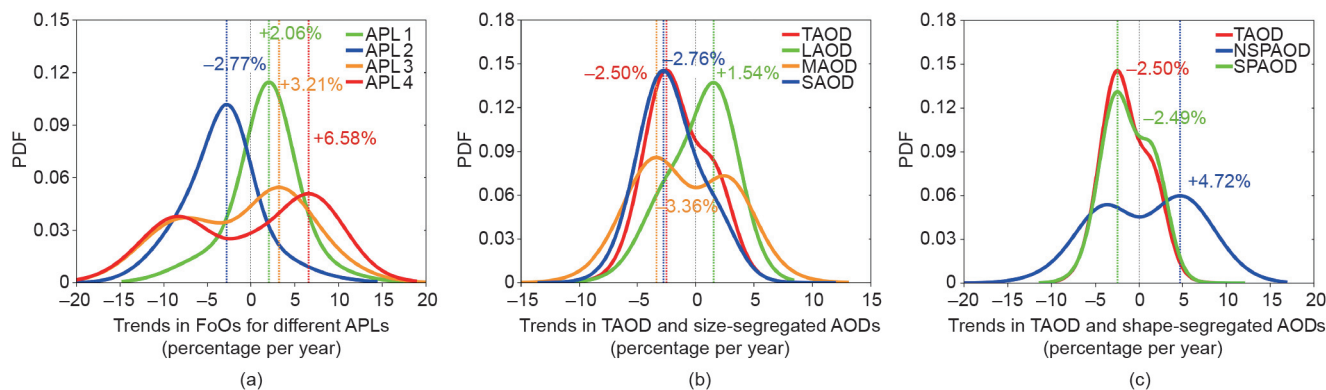
**Fig. 3.** Probability density functions (PDFs) of trends in (a) APLs, (b) TAOD and size-segregated AODs, and (c) TAOD and shape-segregated AODs. The colored dotted lines indicate the peak position of the PDF for each independent variable, while the magnitude of the corresponding value of the PDF peak is indicated by a color-coded number. Note that only grid cells that pass the 95% significance level test are applied in these statistics.
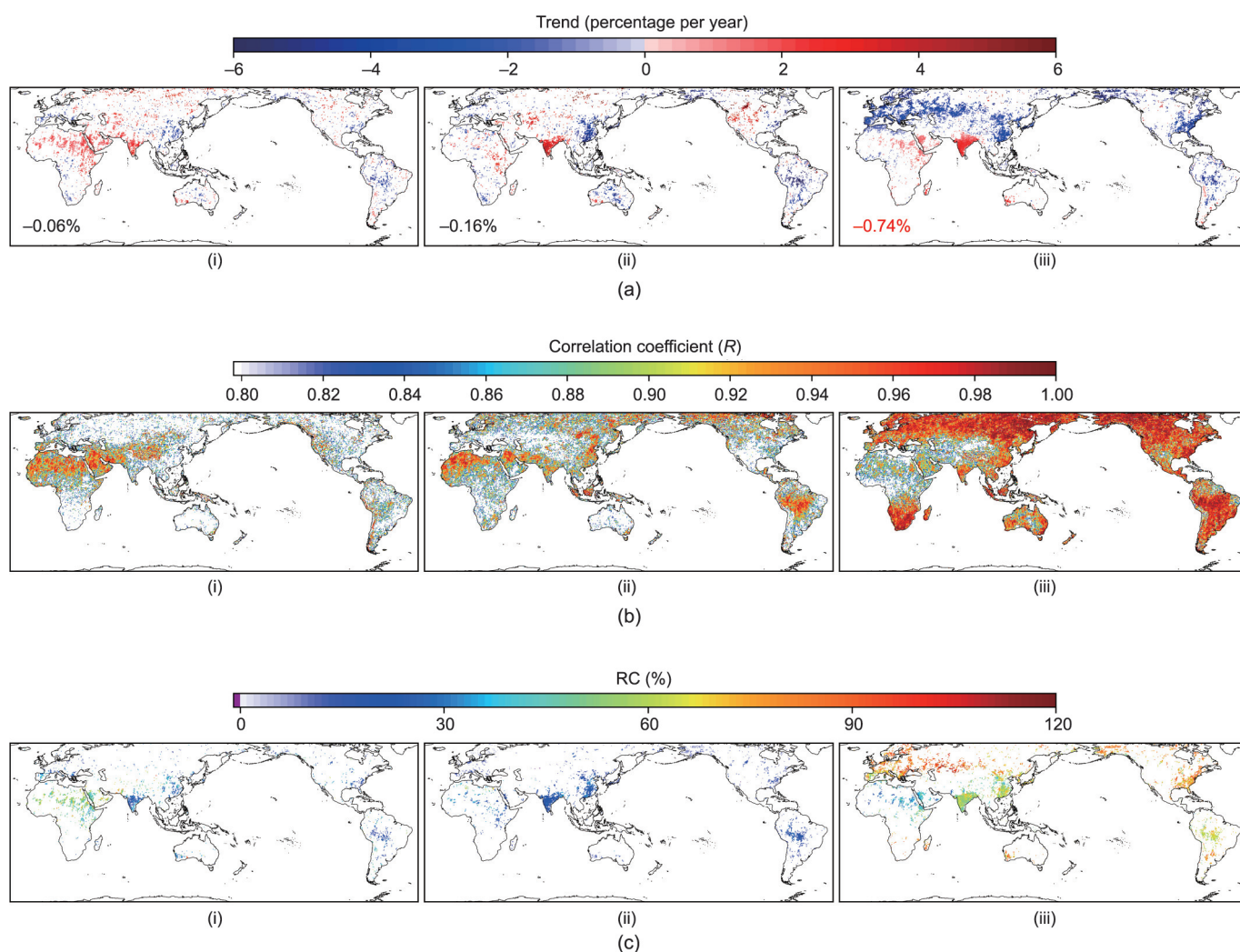


**Fig. 4.** (a) Annual trends (percentage per year) in size-segregated AODs. Note that all trends are expressed as percentage changes: $\frac{Slope}{y} \times 100\%$. Only grids with trend values above the 95% significance level from the M–K test are shown. The number in the lower left of each panel represents the trend value calculated from the time series of the land average. Numbers marked in red indicate that the trend values are above the 95% significance level from the M–K test. (b) The $R$ between size-segregated AODs trends and TAOD changes. (c) RCs of size-segregated AODs to TAOD changes. Note that the RCs are only shown when the trends for TAOD and size-segregated AODs are significant simultaneously. (i) LAOD; (ii) MAOD; and (iii) SAOD.

whereas some significant increases (2%–4% per year) were observed in SAS, the MDE, and central and eastern NAF, consistent with previous studies of trends in TAOD [23,50,51]. These signifi-

cant regional trends were also confirmed by an intercomparison between the estimated trend values from four different AOD data-sets (including two based on satellite retrievals: MODIS/Terra and

MODIS/Aqua; and two based on aerosol value reanalysis: MERRA-2 and CAMS) (Fig. S6 in Appendix A). The high $R$ between MISR and these four different datasets further confirms the consistency among the different AOD datasets (Fig. S7 in Appendix A).

Examination of the trends in size-segregated AODs shows a similar distribution characteristic, but the magnitudes of these trends were not completely consistent. Overall, the decrease in all size-segregated AODs contributed to the decrease in TAOD (Fig. 4(a)), with SAOD showing the most noticeable decline of −0.74%·a$^{-1}$ ($P$ < 0.05) on a land average among all size-segregated AODs (see also Fig. S8(a) in Appendix A). The estimated trends in shape-segregated AODs indicate that these small-sized aerosols with dominant driving roles tended to be spherical particles, as a highly similar spatial distribution pattern was observed among the trends (Fig. S9(a-i) in Appendix A). Moreover, the insignificant interannual variation of NSPAOD on land indirectly confirms this finding (Fig. S9(a-ii)). For the LAODs, the areas with positive trends were located primarily over central and eastern NAF, the MDE, SAS, western NAM, and North and Central RUS. The similar upward trend in TAOD and LAOD in the dust-source areas suggests that large-sized aerosols are the dominant aerosol type driving the trend of total aerosols in these regions. This suggestion is also supported by the high $R$ (0.8–0.9) between TAOD and LAOD and NSPAOD in these regions (Fig. 4(b-i) and Fig. S9(b-ii)). Compared with LAODs, the trends in MAOD showed a similar distribution pattern in all regions except Central Africa and the MDE, but their intensity was intensified considerably, especially in SAS. The correlation analysis shows that the dominant role of medium-sized aerosols on the interannual variability of TAOD was significantly dispersed in space compared with that of large-sized aerosols. In contrast, we found that the trend in SAODs remains highly consistent with that in TAODs in terms of both spatial pattern and magnitude (Fig. 4(a-iii) and Fig. S5), particularly in anthropogenic-aerosol-dominant regions, which suggests that small-sized aerosols emitted by anthropogenic activities are the most dominant aerosol type driving the variation in land TAOD. The almost complete overlapping PDFs between TAOD and SAOD and SPAOD suggest that small-sized and spherical aerosol particles were the dominant aerosol type driving the significant decrease in TAOD over land between 2003 and 2018, rather than aerosol types such as mineral dust associated with NSPAOD, LAOD, and MAOD (Figs. 3(b) and (c)). In addition, the decrease of TAOD is weakened by the rightward shift of the PDF of the trend in LAOD due to the increase in dust aerosols emitted from the majority of dust-source areas. Small-sized spherical aerosol particles show significant decreasing trends to varying degrees, which are mainly related to the continuous decrease in anthropogenic aerosols (from EAS, eastern NAM, and EUR) [22,23,47,52] and natural dust aerosols (from the Taklamakan and Gobi Deserts) in the upstream regions in the past decade [53–55].

### 3.4. RC of type-dependent AODs to TAOD trends

#### 3.4.1. Land RC maps

Using Eq. (3), the annual RCs of each type-segregated AOD were separately calculated for each 0.5° × 0.5° grid box for the whole of the 2003–2018 period; the results are shown in Fig. 4(c) and Fig. S9(c). During the period 2003–2018, the RCs of LAOD and MAOD were similar in spatial distribution, with approximately 10%–30%, except for NAF (RCs of about 50%–60% and 20%–40% for LAOD and MAOD). In contrast, the RCs of SAOD reached the maximum in NAM and EUR with values of about 80%–90%, followed by SAS, EC, and SAM with values about 50%–70%; the lowest values were in NAF and the MDE, at about 30%–40%. The similar distribution of RCs for size-segregated AODs in SAS and EC suggests that the trends of TAOD in these two regions were controlled by

complex aerosol sources [56,57], with both anthropogenic and natural aerosols playing different roles, although the former was more dominant. This suggestion is further confirmed by the significant positive correlation between the MISR-derived TAOD and the anthropogenic and natural aerosols extracted from the CAMS reanalysis (Fig. S10 in Appendix A). The RCs of the shape-segregated AOD demonstrate that the trend in TAOD was mainly driven by SPAOD, while the contribution of NSPAOD was almost negligible or even played a negative role, for example in SAS and Central RUS (Fig. S9(c)).

#### 3.4.2. Regional trends and NRCs

Fig. 5 presents the trends in TAOD and type-segregated AOD over land and the 14 SRs, and the NRCs of these type-separated AODs to TAOD trends. These statistics were based on a time series of regional averages. Globally, the significant decrease in TAOD over land was mainly attributed to the decrease in small-sized and spherical aerosol particles with NRCs of 82.6% and 90.4%, respectively. This finding suggests that the driving role of small-sized and spherical aerosols is dominant, as these NRSs are significantly higher than their proportion in the multi-year average of TAOD (Fig. 1(b)). The $R$s between SAOD and SPAOD and anthropogenic fine-mode AOD (ANT_FM_AOD) were spatially highly similar to those between TAOD and ANT_FM_AOD (Fig. S10(a)), indicating that small-sized and spherical aerosols are mainly composed of SU, OM, and BC produced by anthropogenic and biomass-burning emissions. To elucidate the role of aerosol components, we further decomposed the regional NRCs of the five composition-dependent AODs from the CAMS reanalysis, as shown in Fig. S11 in Appendix A. The results show that SU and OM together explain almost 74.0% of the global variability in land TAOD, whereas natural aerosols (DU and SS) account for slightly less than 20.0%. Regionally, the NRCs of OM are overwhelmingly dominant in EAS, SAS, and SAM, with NRCs of 58.8%, 50.4% and 77.9%, respectively. In contrast, the dominant role of SU is more prevalent in NAM (63.9%) and EUR (52.0%). The dominant driving role of anthropogenic aerosols in the interannual variability of regional TAOD has also been widely confirmed by previous studies. For example, Che et al. [23] showed, based on statistical models, that SU precursor (SO$_2$) and carbonaceous aerosols are the dominant emission drivers explaining the inter-decadal variability of TAOD over typical anthropogenic-aerosol-dominant and biomass-burning-dominant regions, respectively. In addition, Che et al. [23] revealed the non-negligible contribution of meteorological factors to inter-decadal changes in regional aerosol loading. Although it is undoubtedly crucial to explore the complex mechanisms of the meteorological factors influencing aerosol types, this goes beyond the scope of this study.

Among the 14 SRs, TAOD showed a significant positive trend (0.96%·a$^{-1}$, $P$ < 0.05) only in SAS (Fig. 5(a)). The significant increases in all size-segregated AODs and SPAOD were responsible for this trend. Regional NRCs suggest that LAOD, MAOD, SAOD, and SPAOD explained 28.8%, 20.5%, 50.8%, and 88.3% of the TAOD trend in SAS, respectively. In contrast, TAOD exhibited a significant negative trend in EAS, EUR, and CAS, with a trend intensity of –1.49%, –1.65%, and –0.69% per year, respectively. Of these, the decrease of TAOD in EUR (CAS) was closely related to the decreases in MAOD (SAOD), SAOD (SPAOD), and SPAOD (NSPAOD), with NRCs of 3.9% (77.8%), 88.9% (84.8%), and 96.4% (15.2%), respectively. In contrast, the significant reduction of all type-separated AODs contributed significantly to the decrease of TAOD in EAS. In terms of NRCs for size-segregated AODs, the maximum NRCs occurred at SAOD (68.2%), followed by MAOD (17.4%), and the minimum occurred at LAOD (14.4%). For the NRCs of shape-segregated AODs, SPAOD and NSPAOD contributed 89.7% and 10.3% of the decreasing trend of TAOD in EAS, respectively.
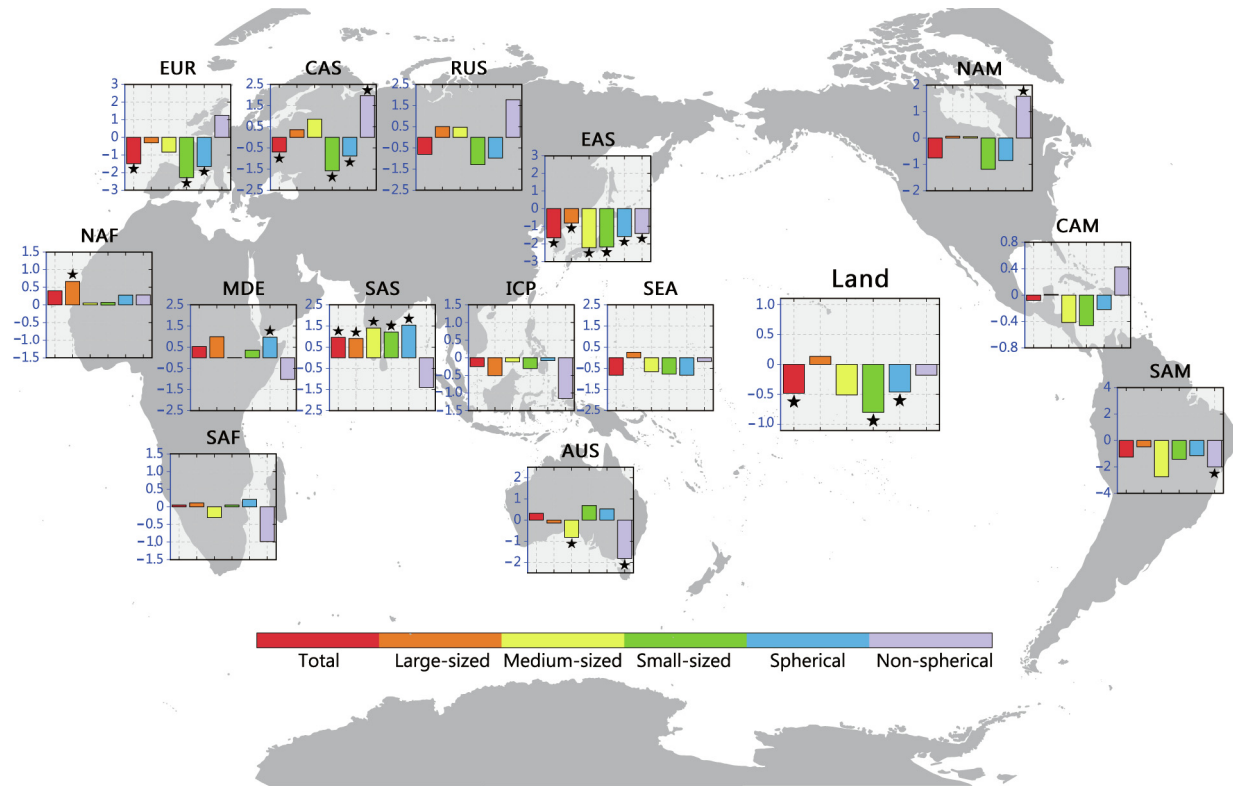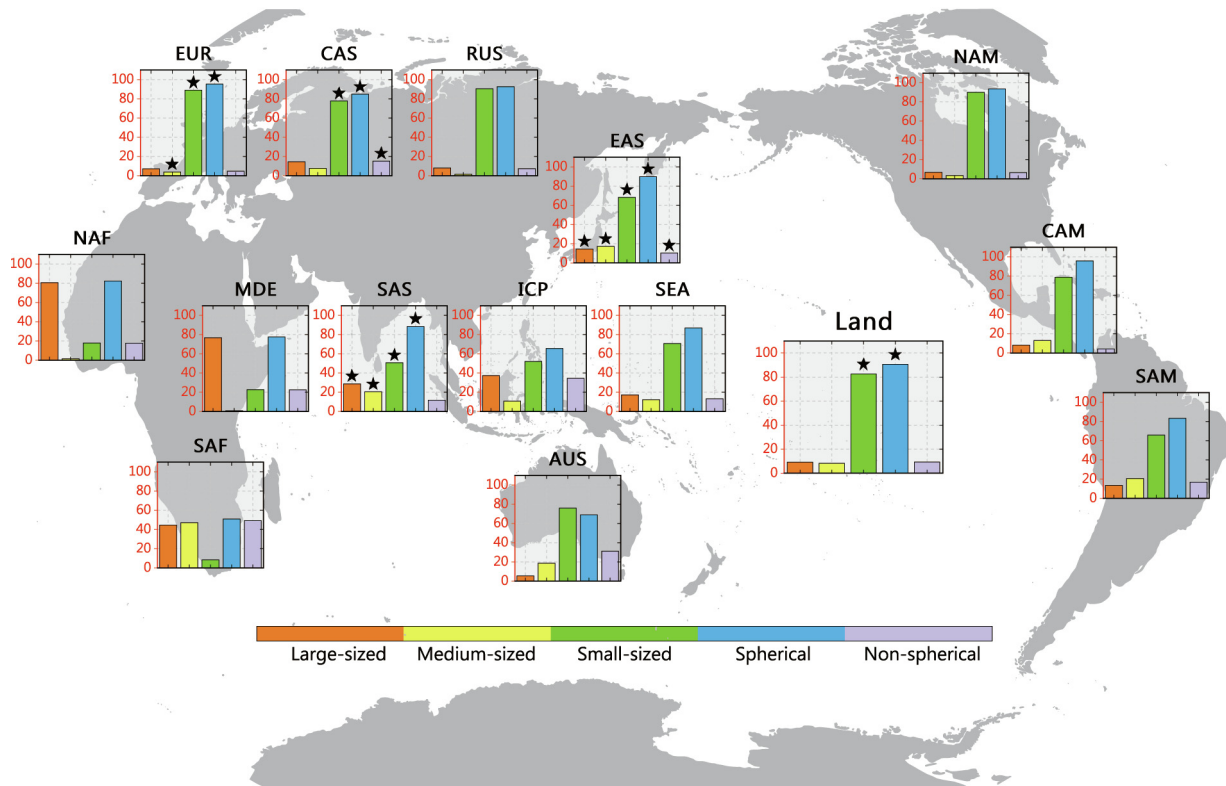
**Fig. 5.** (a) Regional annual trends (i.e., Sen's slope; percentage per year) in TAOD and type-dependent AODs calculated from the time series of regional annual averages during 2003–2018. An asterisk above each bar indicates that the trend value is above the 95% significance level from the M–K test. (b) Regional NRCs (%) of type-dependent AODs to TAOD changes. An asterisk above each bar indicates that the NRC is above the 95% significance level from the two-tailed Student's t-tests.

## 4. Conclusions

This study investigated the decadal-scale trends in type-dependent AODs related to aerosol particle properties using long-term (2003–2018) aerosol optical component dataset retrievals from MISR over land and 14 SRs. Subsequently, we further analyzed the relationships between TAOD trends and type-dependent AOD changes and quantified the RC of each type-dependent AOD to TAOD trends. On average, LAOD, MAOD, SAOD, SPAOD, and NSPAOD contributed 32.2%, 10.3%, 57.5%, 89.6%, and 10.4%, respectively, to the land TAOD. Trend analyses showed that TAOD experienced a global $0.47\%\cdot a^{-1}$ decrease ($P < 0.05$) over land from 2003 to 2018. Spatially, these significant negative trends were mainly located in northwest and eastern NAM, Central SAM, EUR, and EC and adjacent seas, consistent with previous studies of trends in TAOD. Examination of the trends in size-segregated AODs further revealed that this significant reduction is mainly attributed to the continued reduction in SAOD ($-0.74\%\cdot a^{-1}$) and SPAOD ($-0.46\%\cdot a^{-1}$). In addition to diagnosing these trends, the RC of each type-segregated AOD to the trend in TAOD was independently quantified. We found that TAOD changes are primarily controlled by changes in SAOD and SPAOD, which contributed 82.6% and 90.4% of the trends in land TAOD during 2003–2018, respectively, indicating the non-negligible globally dominant role of small-sized and spherical aerosols. The CAMS reanalysis revealed that these dominant aerosol types are mainly composed of SU, OM, and BC from anthropogenic and biomass-burning emissions.

When TAODs were categorized into the four APLs, their FoOs tended to decrease progressively with increasing aerosol burdens. Globally, the multi-year averaged FoOs for APLs 1–4 over land were 63.1%, 26.9%, 8.5%, and 1.6%, respectively. Globally, we observed a 0.238% (0.209%)$\cdot a^{-1}$ ($P < 0.05$) increase (decrease) in FoO in APL 1 (APL 2) over land during 2003–2018. In addition, the PDF distribution of the FoOs at different APLs revealed that air quality improved dramatically in most land areas during 2003–2018, except in SAS. Overall, APLs experienced a shift from a lightly polluted to clean condition. Furthermore, we found that the effects of FoOs at different APLs on the interannual variability of TAOD are complex and strongly regionally dependent. In general, changes in APL 1 had negligible effects on the interannual evolution of TAOD in dust-source and high-anthropogenic-emission regions; instead, it was mainly influenced by the FoOs for APLs 2–4.

Our study indicates that small-sized and spherical aerosols composed of anthropogenic aerosols play a dominant role in determining interannual variability in land TAOD. However, there are some limitations in this study. For example, the influence of the uncertainty in particle types derived from the MISR sensor on the quantification results is not clear. Limited by the sampling frequency, MISR does not have the ability to provide daily global coverage, which may constrain the representativeness of the daily average AOD retrieved from MISR, as atmospheric aerosols usually have noticeable diurnal variability [58,59]. To address this limitation, future work needs to rely on geostationary satellites to improve the characterization of the diurnal variability of regional TAOD. Moreover, whether the significant contribution of small-sized and spherical aerosol particles to the decreasing trend in TAOD over land is attributable to the concentration of aerosols or to the degree of extinction needs to be further explored. Regardless, satellite retrievals of the optical properties of type-dependent aerosols contribute to a more systematic and in-depth understanding of aerosol changes on global and regional scales, especially to their particle size and morphology, as these properties are often closely associated with changes in both anthropogenic and natural aerosols. More importantly, compared with most pre-vious trend studies using isolated TAOD, the dominant driving role of small-sized and spherical aerosol particles that was revealed in this study provides new insights into our knowledge of global aerosol evolution patterns. Given the dominant driving role of anthropogenic aerosols in TAOD variability, future studies should pay more attention to the influence of changes in the chemical components of anthropogenic aerosols and their microphysical properties on inter-decadal changes in TAOD.

## Compliance with ethics guidelines

Ke Gui, Huizheng Che, Lei Li, Yu Zheng, Lei Zhang, Hujia Zhao, Junting Zhong, Wenrui Yao, Yuanxin Liang, Yaqiang Wang, and Xiaoye Zhang declare that they have no conflict of interest or financial conflicts to disclose.

## Appendix A. Supplementary data

Supplementary data to this article can be found online at https://doi.org/10.1016/j.eng.2021.05.017.

## References

[1] Kaufman YJ, Koren I. Smoke and pollution aerosol effect on cloud cover. Science 2006;313:655–8.
[2] Ramanathan V, Carmichael G. Global and regional climate changes due to black carbon. Nat Geosci 2008;1(4):221–7.
[3] Koren I, Altaratz O, Remer LA, Feingold G, Martins JV, Heiblum RH. Aerosol-induced intensification of rain from the tropics to the mid-latitudes. Nat Geosci 2012;5(2):118–22.
[4] Li Z, Lau WKM, Ramanathan V, Wu G, Ding Y, Manoj MG, et al. Aerosol and monsoon climate interactions over Asia. Rev Geophys 2016;54(4):866–929.
[5] Yang Y, Russell LM, Lou S, Liao H, Guo J, Liu Y, et al. Dust–wind interactions can intensify aerosol pollution over eastern China. Nat Commun 2017;8(1):15333.
[6] Jiang JH, Su H, Huang L, Wang Y, Massie S, Zhao B, et al. Contrasting effects on deep convective clouds by different types of aerosols. Nat Commun 2018;9(1):3874.
[7] Huang X, Ding A, Wang Z, Ding K, Gao J, Chai F, et al. Amplified transboundary transport of haze by aerosol–boundary layer interaction in China. Nat Geosci 2020;13(6):428–34.
[8] Xu Y, Liu Y, Han Z, Zhou B, Ding Y, Wu J, et al. Influence of human activities on wintertime haze-related meteorological conditions over the Jing–Jin–Ji region. Engineering 2021;7(8):1185–92.
[9] Ding Y, Wu P, Liu Y, Song Y. Environmental and dynamic conditions for the occurrence of persistent haze events in north China. Engineering 2017;3(2):266–71.
[10] Liu C, Gao M, Hu Q, Brasseur GP, Carmichael GR. Stereoscopic monitoring: a promising strategy to advance diagnostic and prediction of air pollution. Bull Am Meteorol Soc 2021;102(4):1–19.
[11] Xing C, Liu C, Wang S, Chan KL, Gao Y, Huang X, et al. Observations of the vertical distributions of summertime atmospheric pollutants and the

corresponding ozone production in Shanghai, China. Atmos Chem Phys 2017;17(23):14275–89.

[12] Xue T, Zhu T, Zheng Y, Zhang Q. Declines in mental health associated with air pollution and temperature variability in China. Nat Commun 2019;10:2165.

[13] Lelieveld J, Evans JS, Fnais M, Giannadaki D, Pozzer A. The contribution of outdoor air pollution sources to premature mortality on a global scale. Nature 2015;525(7569):367–71.

[14] Liu H, Long Z, Duan Z, Shi H. A new model using multiple feature clustering and neural networks for forecasting hourly $PM_{2.5}$ concentrations, and its applications in China. Engineering 2020;6(8):944–56.

[15] Hu J, Huang L, Chen M, Liao H, Zhang H, Wang S, et al. Premature mortality attributable to particulate matter in China: source contributions and responses to reductions. Environ Sci Technol 2017;51(17):9950–9.

[16] Gui K, Che H, Chen Q, Zeng Z, Zheng Yu, Long Q, et al. Water vapor variation and the effect of aerosols in China. Atmos Environ 2017;165:322–35.

[17] Koren I, Martins JV, Remer LA, Afargan H. Smoke invigoration versus inhibition of clouds over the amazon. Science 2008;321(5891):946–9.

[18] Zhao B, Jiang JH, Diner DJ, Su H, Gu Yu, Liou KN, et al. Intra-annual variations of regional aerosol optical depth, vertical distribution, and particle types from multiple satellite and ground-based observational datasets. Atmos Chem Phys 2018;18(15):11247–60.

[19] Liu Y, Hua S, Jia R, Huang J. Effect of aerosols on the ice cloud properties over the Tibetan Plateau. J Geophys Res Atoms 2019;124(16):9594–608.

[20] Pozzer A, de Meij A, Yoon J, Tost H, Georgoulias AK, Astitha M. AOD trends during 2001–2010 from observations and model simulations. Atmos Chem Phys 2015;15(10):5521–35.

[21] Zhao B, Jiang JH, Gu Y, Diner D, Worden J, Liou KN, et al. Decadal-scale trends in regional aerosol particle properties and their linkage to emission changes. Environ Res Lett 2017;12(5):054021.

[22] Hammer MS, Martin RV, Li C, Torres O, Manning M, Boys BL. Insight into global trends in aerosol composition from 2005 to 2015 inferred from the OMI ultraviolet aerosol index. Atmos Chem Phys 2018;18(11):8097–112.

[23] Che H, Gui K, Xia X, Wang Y, Holben BN, Goloub P, et al. Large contribution of meteorological factors to inter-decadal changes in regional aerosol optical depth. Atmos Chem Phys 2019;19(16):10497–523.

[24] Li L, Che H, Derimian Y, Dubovik O, Luan Q, Li Q, et al. Climatology of fine and coarse mode aerosol optical thickness over East and South Asia derived from POLDER/PARASOL satellite. J Geophys Res Atmos 2020;125(16): e2020JD032665.

[25] Stocker TF, Qin D, Plattner GK, Tignor MMB, Allen SK, Boschung J, editors. Climate change 2013 the physical science basis. Working Group I Contribution to the Fifth Assessment Report of the Intergovernmental Panel on Climate Change. Cambridge: Cambridge University Press; 2013.

[26] Diner DJ, Beckert JC, Reilly TH, Bruegge CJ, Conel JE, Kahn RA, et al. Multi-Angle Imaging Spectroradiometer (MISR) instrument description and experiment overview. IEEE Trans Geosci Remote Sens 1998;36(4):1072–87.

[27] Kahn R, Banerjee P, McDonald D. Sensitivity of multiangle imaging to natural mixtures of aerosols over ocean. J Geophys Res Atmos 2001;106 (D16):18219–38.

[28] Garay MJ, Witek ML, Kahn RA, Seidel FC, Limbacher JA, Bull MA, et al. Introducing the 4.4 km spatial resolution multi-angle imaging spectroradiometer (MISR) aerosol product. Atmos Meas Tech 2020;13(2):593–628.

[29] Diner DJ, Martonchik JV, Kahn RA, Pinty B, Gobron N, Nelson DL, et al. Using angular and spectral shape similarity constraints to improve MISR aerosol and surface retrievals over land. Remote Sens Environ 2005;94(2):155–71.

[30] Kahn RA, Gaitley BJ, Garay MJ, Diner DJ, Eck TF, Smirnov A, et al. Multiangle imaging spectroradiometer global aerosol product assessment by comparison with the aerosol robotic network. J Geophys Res Atmos 2010;115:D23209.

[31] Kahn RA, Gaitley BJ. An analysis of global aerosol type as retrieved by MISR. J Geophys Res 2015;120(9):4248–81.

[32] Kahn R, Petzold A, Wendisch M, Bierwirth E, Dinter T, Esselborn M, et al. Desert dust aerosol air mass mapping in the western Sahara, using particle properties derived from space-based multi-angle imaging. Tellus B Chem Phys Meteror 2009;61(1):239–51.

[33] Inness A, Ades M, Agustí-Panareda A, Barré J, Benedictow A, Blechschmidt AM, et al. The CAMS reanalysis of atmospheric composition. Atmos Chem Phys 2019;19(6):3515–56.

[34] Buchard V, Randles CA, da Silva AM, Darmenov A, Colarco PR, Govindaraju R, et al. The MERRA-2 aerosol reanalysis, 1980-onward, part I: system description and data assimilation evaluation. J Clim 2017;30:6851–72.

[35] Mann HB. Nonparametric tests against trend. Econometrica 1945;13 (3):245–59.

[36] Kendall MG. Rank correlation methods. 4th ed. London: Charles Griffin; 1975.

[37] Xu C, Ma Y, Yang K, You C. Tibetan Plateau impacts on global dust transport in the upper troposphere. J Clim 2018;31(12):4745–56.

[38] Zhu J, Xia X, Che H, Wang J, Cong Z, Zhao T, et al. Spatiotemporal variation of aerosol and potential long-range transport impact over the Tibetan Plateau, China. Atmos Chem Phys 2019;19(23):14637–56.

[39] Zhao C, Yang Y, Fan H, Huang J, Fu Y, Zhang X, et al. Aerosol characteristics and impacts on weather and climate over the Tibetan Plateau. Natl Sci Rev 2020;7 (3):492–5.

[40] Zubkova M, Boschetti L, Abatzoglou JT, Giglio L. Changes in fire activity in Africa from 2002 to 2016 and their potential drivers. Geophys Res Lett 2019;46 (13):7643–53.

[41] David LM, Ravishankara AR, Kodros JK, Venkataraman C, Sadavarte P, Pierce JR, et al. Aerosol optical depth over India. J Geophys Res Atmos 2018;123 (7):3688–703.

[42] Koren I, Remer LA, Longo K. Reversal of trend of biomass burning in the Amazon. Geophys Res Lett 2007;34(20):2–5.

[43] Hammer MS, van Donkelaar A, Li C, Lyapustin A, Sayer AM, Hsu NC, et al. Global estimates and long-term trends of fine particulate matter concentrations (1998–2018). Environ Sci Technol 2020;54(13):7879–90.

[44] Zhang F, Wang Y, Peng J, Chen L, Sun Y, Duan L, et al. An unexpected catalyst dominates formation and radiative forcing of regional haze. Proc Natl Acad Sci USA 2020;117(8):3960–6.

[45] Zhang C, Liu C, Hu Q, Cai Z, Su W, Xia C, et al. Satellite UV–Vis spectroscopy: implications for air quality trends and their driving forces in China during 2005–2017. Light Sci Appl 2019;8(1):100.

[46] Zhang C, Liu C, Chan KL, Hu Q, Liu H, Li B, et al. First observation of tropospheric nitrogen dioxide from the environmental trace gases monitoring instrument onboard the GaoFen-5 satellite. Light Sci Appl 2020;9(1):66.

[47] Zhang Q, Zheng Y, Tong D, Shao M, Wang S, Zhang Y, et al. Drivers of improved $PM_{2.5}$ air quality in China from 2013 to 2017. Proc Natl Acad Sci USA 2019;116 (49):24463–9.

[48] Xie M, Duan H, Kang P, Qiao Q, Bai L. Toward an ecological civilization: China's progress as documented by the second national general survey of pollution sources. Engineering 2021;7(9):1336–41.

[49] Lu X, Zhang S, Xing J, Wang Y, Chen W, Ding D, et al. Progress of air pollution control in China and its challenges and opportunities in the ecological civilization era. Engineering 2020;6(12):1423–31.

[50] Klingmüller K, Pozzer A, Metzger S, Stenchikov GL, Lelieveld J. Aerosol optical depth trend over the Middle East. Atmos Chem Phys 2016;16(8):5063–73.

[51] Jin Q, Pryor SC. Long-term trends of high aerosol pollution events and their climatic impacts in north America using multiple satellite retrievals and modern-era retrospective analysis for research and applications version 2. J Geophys Res Atmos 2020;125(4): e2019JD031137.

[52] Zheng B, Tong D, Li M, Liu F, Hong C, Geng G, et al. Trends in China's anthropogenic emissions since 2010 as the consequence of clean air actions. Atmos Chem Phys 2018;18(19):14095–111.

[53] Wang X, Liu J, Che H, Ji F, Liu J. Spatial and temporal evolution of natural and anthropogenic dust events over northern China. Sci Rep 2018;8(1):2141.

[54] Liu J, Wu D, Liu G, Mao R, Chen S, Ji M, et al. Impact of Arctic amplification on declining spring dust events in East Asia. Clim Dyn 2020;54(3–4):1913–35.

[55] Yao W, Gui K, Wang Y, Che H, Zhang X. Identifying the dominant local factors of 2000–2019 changes in dust loading over East Asia. Sci Total Environ 2021;777:146064.

[56] Zhou D, Ding K, Huang X, Liu L, Liu Q, Xu Z, et al. Transport, mixing and feedback of dust, biomass burning and anthropogenic pollutants in eastern Asia: a case study. Atmos Chem Phys 2018;18(22):16345–61.

[57] Sun T, Che H, Qi B, Wang Y, Dong Y, Xia X, et al. Aerosol optical characteristics and their vertical distributions under enhanced haze pollution events: effect of the regional transport of different aerosol types over eastern China. Atmos Chem Phys 2018;18(4):2949–71.

[58] Wang J, Xia X, Wang P, Christopher SA. Diurnal variability of dust aerosol optical thickness and Angström exponent over dust source regions in China. Geophys Res Lett 2004;31(8):L08107.

[59] Christopher SA, Wang J. Intercomparison between Multi-Angle Imaging Spectroradiometer (MISR) and sunphotometer aerosol optical thickness in dust source regions over China: implications for satellite aerosol retrievals and radiative forcing calculations. Tellus B Chem Phys Meteror 2004;56(5):451–6.